RSC Advances

ROYAL SOCIETY OF CHEMISTRY

www.rsc.org/advances

TOC Graphic

$Ce_{0.80}Pr_{0.12}Sn_{0.08}O_{2-\delta}$ combination catalyst exhibited highest CO oxidation activity owing to its high specific surface area, better reducibility, superior surface active oxygen species, and oxygen vacancies among various samples investigated.

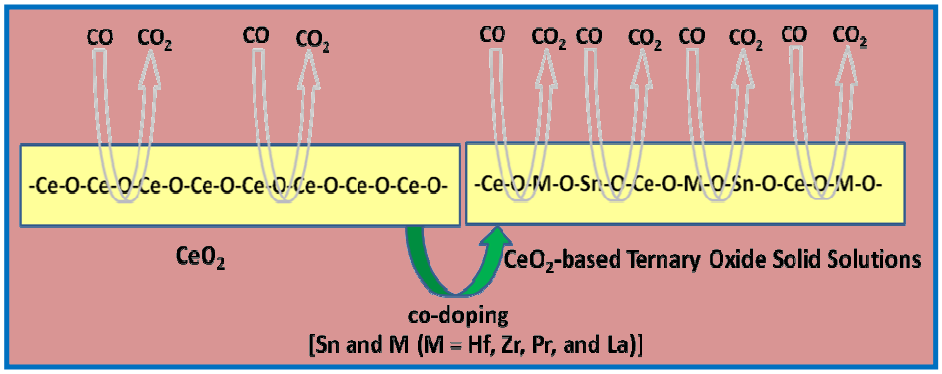

Cite this: DOI: 10.1039/c0xx00000x

www.rsc.org/xxxxxx

ARTICLE TYPE

$Ce_{0.80}M_{0.12}Sn_{0.08}O_{2-\delta}$ (M = Hf, Zr, Pr, and La) ternary oxide solid solutions with superior properties for CO oxidation

Damma Devaiah,[a,b] Takuya Tsuzuki,[b] Thirupathi Boningari,[c] Panagiotis G. Smirniotis,[c]

Benjaram M. Reddy[a,*]

Received (in XXX, XXX) Xth XXXXXXXXX 20XX, Accepted Xth XXXXXXXXX 20XX
DOI: 10.1039/b000000x

To develop efficient materials for CO oxidation, a series of co-doped CeO_2 ternary oxide solid solutions ($Ce_{0.80}M_{0.12}Sn_{0.08}O_{2-\delta}$, M = Hf, Zr, Pr, and La) were prepared by a simple coprecipitation method. The fundamental characteristics of the co-doped CeO_2 samples were studied by X-ray diffraction, Raman spectroscopy, UV-visible diffuse reflectance spectroscopy, transmission electron microscopy, Brunauer–Emmett–Teller surface area, H_2-temperature programmed reduction, X-ray photoelectron spectroscopy, and O_2-temperature programmed desorption. The oxidation of CO was chosen as a model reaction to evaluate the catalytic performance of these samples. The characterization results revealed that ternary oxide solid solutions had significantly enhanced surface area, improved reducibility, increased oxygen mobility and higher quantity of surface adsorbed oxygen species and oxygen vacancies, compared to undoped CeO_2. The CO oxidation performance of CeO_2 was greatly improved upon co-doping due to the modification in structural, textural, and redox properties. Especially, the $Ce_{0.80}Pr_{0.12}Sn_{0.08}O_{2-\delta}$ combination catalyst exhibited the highest oxidation activity among the investigated samples, which is attributed to its high specific surface area, better reducibility, superior surface active oxygen species, and oxygen vacancies among the various samples investigated.

1. Introduction

Carbon monoxide (CO), emitted in large amounts mainly from industrial processes and transportation, is considered as one of the most serious air pollutants that can cause many environmental and health problems. Much research effort has been made to mitigate the toxic character of CO by oxidizing it at low temperatures over heterogeneous metal oxide catalysts.[1] Oxidation of CO is also an ideal model reaction to develop and test novel catalysts due to its simplicity. As such, the catalytic oxidation of CO has gained immense attention in the history of heterogeneous catalysis.

Among the various catalysts reported to be active for CO oxidation, ceria (CeO_2) is considered as one of the most promising candidates because of its unique oxygen storage capacity (OSC) and facile conversion between Ce^{4+} and Ce^{3+} oxidation states.[2,3] However, the high reduction temperature and poor thermal stability of this material limits its practical applications. One effective strategy to tackle these problems is to form ceria-based binary oxide solid solutions by doping with various transition, rare-earth or alkaline-earth elements.[2,4] It was shown that incorporation of these metals into the CeO_2 lattice enhances its redox properties, OSC, and thermal stability.[2] For example, doping of CeO_2 with Zr resulted in the formation of a ceria–zirconia (CZ) solid solution that promoted its Ce^{4+}/Ce^{3+} redox couple, leading to an enhanced OSC, thermal resistance, and better catalytic activity.[5–8] Our previous works also demonstrated that the CO oxidation properties of CeO_2 were improved greatly by doping of Hf, Zr, Pr, or La cations to form the binary oxide solid solutions.[9–11]

Tin is a potentially interesting dopant in ceria-based oxides for oxidation reaction applications, because of its facile reversible conversion between Sn^{4+} and Sn^{2+} states at relatively lower temperatures.[12,13] It is also one of the extensively used oxides in the manufacture of sensors for monitoring the environment.[14,15] Moreover, SnO_2 is an n-type semiconductor with surface oxygen deficiencies and active lattice oxygen species, which are important for catalytic oxidation reactions.[13,16–18] Sasikala *et al*. reported that Ce–Sn mixed oxides exhibit better CO oxidation activity than SnO_2 and CeO_2.[13] Xu and co-workers found that Sn–Ce binary oxide shows improved activity for CO and CH_4 oxidation reactions. Ayastuy *et al*. investigated a series of $Ce_xSn_{1-x}O_{2-\delta}$ oxides for CO oxidation and found that SnO_2 can promote the catalytic activity of CeO_2.[12] They ascribed the good performance due to favourable balance between lattice defects, the OSC, and easy reducibility. These reports suggest that Sn as well as various transition or rare-earth elements improve the properties of CeO_2-based catalysts.

Accordingly, attempts have been made to combine the advantages of various transition or rare-earth elements and tin to prepare further improved CeO_2-based ternary oxide solid solutions by co-doping process. Very few reports could be found

in the literature on the preparation of SnO_2 modified CeO_2-based binary oxide solid solutions as better ternary oxide catalysts. For instance, Dong and co-workers synthesized Sn doped CZ ($Ce_{0.5}Zr_{0.43}Sn_{0.07}O_2$) ternary oxide solid solutions, which exhibited a remarkably higher OSC and excellent thermal stability in comparison with CeO_2 and $Ce_{0.5}Zr_{0.5}O_2$ samples.[19] However, a careful literature survey indicates that no work has been reported previously using Hf or Pr or La together with Sn co-doped CeO_2 ternary oxide solid solutions as catalysts for CO oxidation.

Therefore, the intention of the present work was to prepare Ce–Hf–Sn, Ce–Zr–Sn, Ce–Pr–Sn, and Ce–La–Sn ternary oxide solid solutions by coprecipitation method. The synthesized samples were systematically investigated by X-ray diffraction (XRD), Raman spectroscopy (RS), UV-vis diffuse reflectance spectroscopy (UV-vis DRS), transmission electron microscopy (TEM), Brunauer–Emmett–Teller (BET) surface area, H_2-temperature programmed reduction (H_2-TPR), X-ray photoelectron spectroscopy (XPS), and O_2-temperature programmed desorption (O_2-TPD) measurements. The activity of these catalysts was evaluated for CO oxidation and the corresponding results were compared.

2. Experimental section

2.1 Catalyst preparation

The optimized $Ce_{0.80}Hf_{0.12}Sn_{0.08}O_{2-\delta}$ (CHS), $Ce_{0.80}Zr_{0.12}Sn_{0.08}O_{2-\delta}$ (CZS), $Ce_{0.80}Pr_{0.12}Sn_{0.08}O_{2-\delta}$ (CPS), and $Ce_{0.80}La_{0.12}Sn_{0.08}O_{2-\delta}$ (CLS) (mol ratio based on oxides) ternary oxide solid solutions were synthesized by a coprecipitation method. In detail, the desired quantities (*see* Table S1, ESI†) of $Ce(NO_3)_3{\cdot}6H_2O$, $SnCl_4{\cdot}5H_2O$, and other respective metal precursors such as $HfCl_4$, $ZrO(NO_3)_2{\cdot}xH_2O$, $Pr(NO_3)_3{\cdot}6H_2O$, and $La(NO_3)_3{\cdot}6H_2O$ were dissolved in distilled water separately and then mixed together for 1 h. Under constant stirring, aqueous ammonia solution was added dropwise to the mixture until the precipitation was complete, at which point the pH was approximately 9.0. The resulting suspensions were stirred for another 12 h, aged for 24 h and then vacuum filtered. Afterwards, the precipitates were washed thoroughly with distilled water and the obtained solids were dried at 373 K overnight and finally calcined at 773 K for 5 h. For comparison, the same synthesis route was employed for the preparation of CeO_2.

2.2 Catalyst characterization

X-ray diffraction patterns were performed on a Rigaku Multiflex diffractometer equipped with a nickel-filtered Cu-Kα (1.5418 Å) radiation source and a scintillation counter detector. The diffraction data were collected over a 2θ range of 20–80° with a step size of 0.02º. Phase identification was carried out by comparison with JCPDF database cards. The mean crystallite size (D) was calculated by the Scherrer equation. The lattice parameter was calculated by a standard cubic indexation method with the intensity of the most prominent peaks using the relation of $a = d(h^2 + k^2 + l^2)^{1/2}$, where '*a*' is the lattice parameter and 'd' is the interplanar spacing calculated from the Bragg equation.

The Raman spectra were obtained at room temperature using a LabRam HR800UV Raman spectrometer (Horiba Jobin-Yvon) fitted with a confocal microscope and liquid-nitrogen cooled charge-coupled device (CCD) detector. Samples were excited with the emission line at 632 nm from an Ar^+ ion laser (Spectra Physics) which was focused on the sample under the microscope with the diameter of the analyzed spot being ~1 μm. The acquisition time was adjusted according to the intensity of Raman scattering. The wave number values obtained from the spectra were precise to within 2 cm^{-1}. The UV-visible diffuse reflectance spectroscopy measurements were performed by using a GBSCintra 10e UV-vis NIR spectrophotometer with an integration sphere diffuse reflectance attachment. $BaSO_4$ was used as the reference and spectra were recorded in the range 200–800 nm.

Transmission electron microscopy studies were carried out on a JEM-2100 (JEOL) microscope equipped with a slow-scan CCD camera and at an accelerating voltage of 200 kV. Samples for TEM analysis were prepared by crushing the materials in an agate mortar and dispersing them ultrasonically in ethyl alcohol for 5 min. Afterward, a drop of the dilute suspension was placed on a perforated-carbon-coated copper grid and allowed to dry by evaporation at ambient temperature. The elemental analysis was carried out on TEM-EDX analysis. The BET surface areas were determined by N_2 physisorption at liquid N_2 temperature on a Micromeritics Gemini 2360 instrument using a thermal conductivity detector (TCD). Prior to analysis, the samples were degassed at 393 K for 2 h to remove the surface adsorbed residual moisture.

The reducibility of the catalysts was studied by H_2-TPR analysis using a thermal conductivity detector of a gas chromatograph (Shimadzu). Prior to the reduction, approximately 30 mg of the sample was loaded in an isothermal zone of the reactor and pre-treated in a helium gas flow at 473 K and then cooled to room temperature. Then, the sample was heated at a rate of 10 K min^{-1} from ambient temperature to 1100 K in a 20 mL min^{-1} flow of 5% H_2 in Ar. The hydrogen consumption during the reduction process was estimated by passing the effluent gas through a molecular sieve trap to remove the produced water and it was analyzed by gas chromatography using the thermal conductivity detector.

X-ray photoelectron spectroscopy measurements were performed on a Shimadzu ESCA 3400 spectrometer using Mg-Kα (1253.6 eV) radiation as the excitation source at room temperature. The samples were maintained in a strict vacuum typically on the order of less than 10^{-8} Pa to avoid a large amount of noise in the spectra from the contaminants. The obtained binding energies were corrected by referencing the spectra to the carbon (C 1s) peak at 284.6 eV.

O_2-TPD profiles of the catalysts were measured with an AutoChem 2920 II-Micromeritics device. About 100 mg of the sample was used. Prior to the measurement, the sample was cleaned in a He flow for 60 min at 573 K with a heating rate of 5 K/min and then was cooled down to 393 K. Afterward, a flow of 5% O_2/He was passed through the sample for 120 min at 393 K for the adsorption period and then cooled to 373 K temperature. Finally, the temperature was increased with the heating rate of 5 K/min from 373 to 1273 K for 60 min for desorption of the previous adsorbed oxygen. The adsorbed oxygen was calculated from the signal of a TCD detector.

2.3 Catalytic activity studies

The catalytic performance of the samples for CO oxidation was evaluated at atmospheric pressure in the temperature range 300–800 K. About 0.3 g catalyst samples (1 mm mesh size) were supported between glass wool plugs and flanked by inert porcelain beads in the middle of a specially designed quartz reactor. The catalysts were activated at 573 K for 1 h prior to reaction studies. The reactant gases (1% CO, 5% O_2, balanced with 94% N_2) passed through the reactor at a space velocity of 30,000 h^{-1}. The CO and CO_2 in the outlet gas were separated using "Pouropack" packed column, converted to methane by the 'methanator' with SÜD-CHEMIE Ni-catalyst working at 673 K and finally detected separately by online GC-FID.

3. Results and discussion

3.1 Characterization studies

The synthesized CHS, CZS, CPS, and CLS samples along with undoped CeO_2 were analyzed by XRD and the corresponding results are shown in Figure 1 and Table 1. All samples exhibited only the fluorite structure of CeO_2, which is evidenced by the characteristic (111), (200), (220), (311), (222), (400), and (331) peaks. No additional phases corresponding to individual oxides of HfO_2, ZrO_2, Pr_6O_{11}, La_2O_3, and SnO_2 were observed. Moreover, the diffraction peak associated with CeO_2 (111) of CHS, CZS, and CPS samples shifted to higher angles compared to that of undoped CeO_2 (inset Figure 1). In contrast, the diffraction peak of the CLS sample is shifted to lower angle, as compared to the undoped ceria (inset Figure 1). These observations confirm the formation of single phase ternary oxide solid solutions by co-doping of different cations into the CeO_2 lattice.

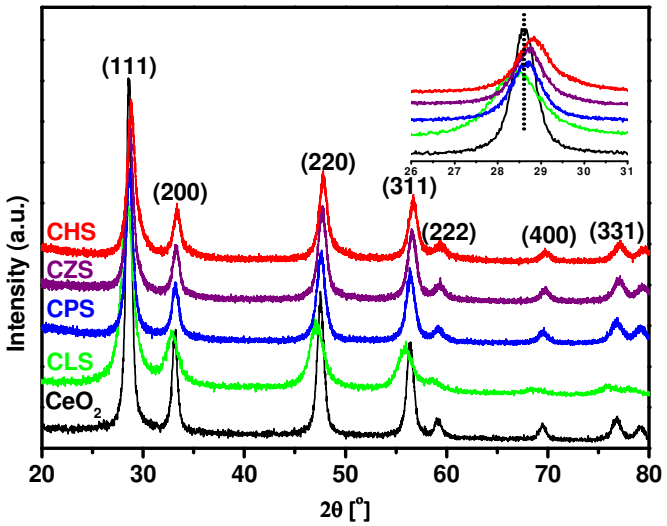

Fig. 1 X-ray diffraction patterns of co-doped CeO_2 and undoped (reference) CeO_2 samples (inset: expanded view of selected region).

As known the lattice parameter strongly depends on the radius of the dopants, as shown in Table 1. It could be noted that the calculated lattice parameters of CHS (0.5359 nm), CZS (0.5376 nm), and CPS (0.5387 nm) samples are smaller than that of CeO_2 (0.5400 nm). The shrinkage of crystal lattices can be due to the smaller ionic radius of respective dopant ions (Hf^{4+} = 0.083 nm, Zr^{4+} = 0.084 nm, Pr^{4+} = 0.096 nm, and Sn^{4+} = 0.081 nm) in relation to Ce^{4+} (0.097 nm). It is interesting that the lattice parameter of CLS sample (0.5427 nm) is higher to that of CeO_2. This result suggests that the lattice expansion due to larger ionic radius of La^{3+} (0.110 nm) dopant than Ce^{4+} slightly prevails with regard to the contraction due to other dopant Sn^{4+}. Therefore, the change in the lattice parameter values in comparison with undoped CeO_2 is again strongly supports the formation of ternary oxide solid solutions. Further, it is found that the crystallite sizes of these samples range from 6.3 to 11.5 nm. The crystallite sizes of spent catalysts were also calculated using XRD data (*see* Figure S1, ESI†). From these values, it is evident that the stability of CPS is higher than the other ternary oxides.

Raman spectroscopy is a powerful technique to identify the effect of co-doping on the structure of the prepared samples after XRD. This is because Raman spectra are dominated by oxygen lattice vibrations and is sensitive to the crystalline symmetry, whereas the XRD results are related to the cation sublattice.[20,21] The Raman spectra of all the samples are shown in Figure 2. All the samples display a main Raman band at 453–467 cm^{-1} assigned to the F_{2g} mode of CeO_2 fluorite-type structure which can be regarded as a symmetric breathing pattern of the oxygen atoms around cerium ions.[21–23]

Further, it can be noticed from Figure 2 that the undoped CeO_2 showed a characteristic peak at 465.4 cm^{-1} whereas the characteristic peak in CLS, CPS, CZS, and CHS samples is shifted to 453.3, 466.1, 466.9, and 467.4 cm^{-1}, respectively. No additional peaks characteristic of dopant oxides were observed, indicating the formation of ternary oxide solid solutions, which is in line with the XRD results. The shift also reflects the lattice distortion related to cell contraction or expansion caused by the difference in ionic radius of respective dopants compared to that of Ce^{4+} (0.097 nm), and is consistent with the lattice parameter values obtained from XRD study.

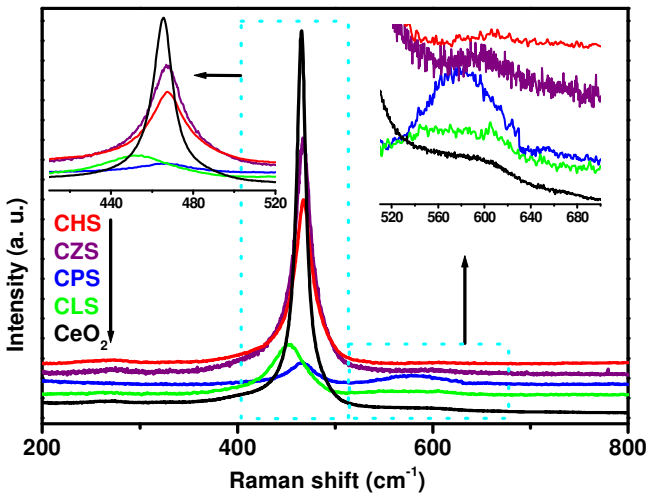

Fig. 2 Raman spectra of co-doped CeO_2 and undoped (reference) CeO_2 samples (inset: expanded view of selected region).

Undoped CeO_2 showed the most intense characteristic peak, indicative of the most ordered structure among those studied. The peak intensity decreased significantly with the addition of dopants in the CeO_2 lattice, which again indicates the deformation of CeO_2 crystal structure by the formation of ternary

oxide solid solutions. This distortion can be attributed to the formation of oxygen vacancies to an enhanced oxygen mobility which will lead to the improvement in the reduction at lower temperatures.[21,24] The order of decrease in the peak intensity was CPS > CLS > CHS > CZS. A strong decrease in the peak intensity in CPS suggests the formation of a higher number of oxygen vacancies in CPS than other samples. Apart from the fluorite peak, an additional peak ranged between ~576 cm^{-1} and ~607 cm^{-1} (inset Figure 2) was also observed in all samples. The relative intensity of this peak was more significant in CPS than in other samples. This peak is attributed to the presence of oxygen vacancies or lattice defects. Hence, the strong peak in CPS again suggests that the presence of more oxygen vacancies, which may cause the highest catalytic activity among the various samples investigated.[23,25,26]

UV-vis DRS was used to obtain information on the surface coordination and electronic states of the metal ions by measuring the d–d and f–d electron transitions and oxygen–metal ion charge transfer bands respectively.[27] The UV-vis DR spectra of all samples are presented in Figure 3. Generally, a split of the absorption into three bands is observed for CeO_2 at 255, 285, and 340 nm, corresponding to the $O^{2-} \rightarrow Ce^{3+}$ and $O^{2-} \rightarrow Ce^{4+}$ charge transfer (CT) and interband transitions (IBT), respectively.[9,28,29] As noticed from the Figure 3, all samples showed a broad absorption band below 400 nm, which can be attributed to the overlap of CT and IBT transitions. Therefore, both Ce^{3+} (oxygen vacancies) and Ce^{4+} ions did exist in these samples. No adsorption band was observed above 400 nm for all samples except CPS that showed an absorption band around at 500 nm due to a Pr^{3+} ion transition.[10,30]

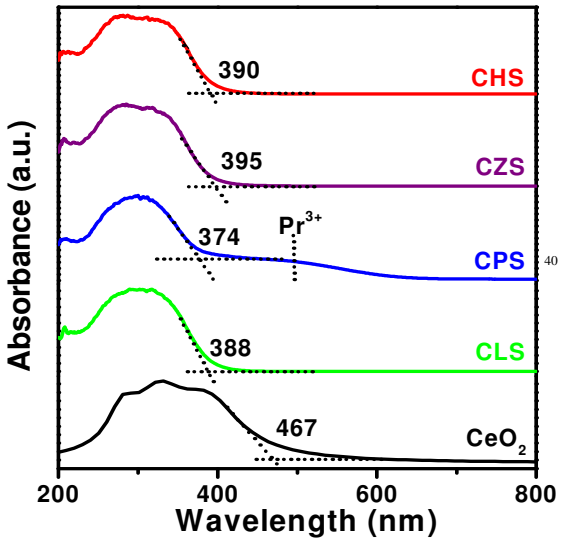

Fig. 3 UV-visible DR spectra of co-doped CeO_2 and undoped (reference) CeO_2 samples.

Furthermore, the absorption edges of CPS, CLS, CHS, and CZS samples are shifted to lower wavelength from 467 nm of undoped CeO_2 to 374, 388, 390, and 395 nm, respectively. This blue shift follows the order CPS > CLS > CHS > CZS. The shift in the absorption edge could be due to the increase in the charge-transfer gap between O 2p and Ce 4f orbitals by a significant increase in the Ce^{3+} fraction on the surface.[10,31] Thus, the largest blue shift of CPS should be related to its higher Ce^{3+} fraction or oxygen vacancies compared to all other samples, in agreement with Raman results, which may improve the catalytic activity.

The morphology and particle size of the CHS, CZS, CPS, and CLS samples were investigated by TEM and the corresponding images are shown in Figure 4. It can be seen that the samples consisted of agglomerates with no distinctive shapes. The mean size of the primary particles was measured to be in the range of 9 to 12 nm, which is in good agreement with the XRD results. The CLS sample exhibits the highest degree of agglomeration which may be attributed to the smallest grain size among these samples. The compositions of the samples were also confirmed by TEM-EDX analysis (Table S2, ESI†).

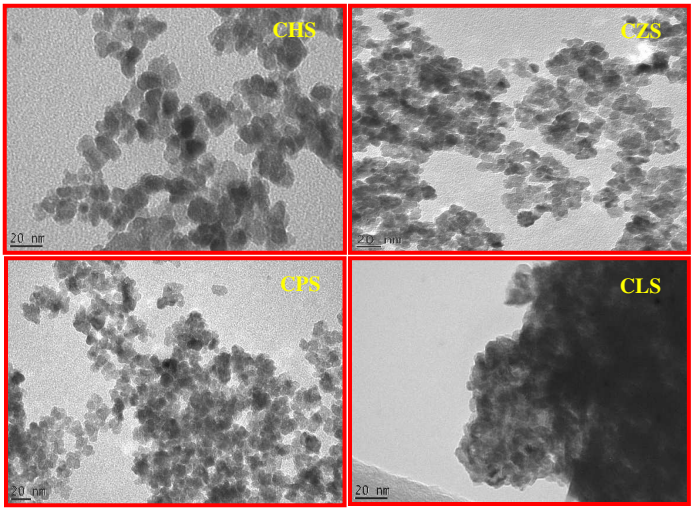

Fig. 4 TEM images of co-doped CeO_2 samples.

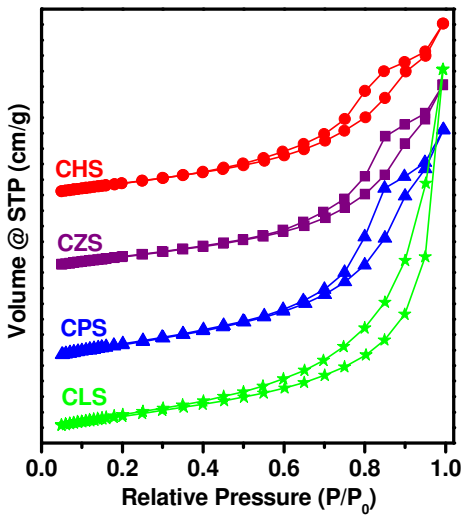

Fig. 5 N_2 adsorption–desorption isotherms of co-doped CeO_2 samples.

The N_2 adsorption–desorption isotherms of various samples are depicted in Figure 5. All the solid solutions exhibited typical type IV adsorption–desorption isotherms with hysteresis loops, indicating the existence of porous structures in the samples. It could be noted that all isotherms show the N_2 capillary condensation in a wide range of relative pressure (P/P_0 = 0.35–

0.97), characteristic of mesoporous structures.[32] These mesoporous structures are probably generated by the inter connections between agglomerates (as evidenced from TEM images) of ternary oxide solid solutions.[33] The textural properties of the samples are summarized in Table 1. Compared with undoped CeO_2, the surface area of CZS, CHS, CLS, and CPS samples increased from 41 to 74, 78, 85, and 95 m^2/g, respectively, indicating that the co-doping can effectively improve the textural property of the CeO_2 which could provide more surface active sites for the CO oxidation reaction. Noticeably, the highest surface area of CPS sample suggests that it may be a good catalyst for CO oxidation among the samples. Further, the pore volume of solid solutions ranges from 0.1384 to 0.1893 cm^3/g.

The influence of the co-doping on the redox property of CeO_2 is probed by H_2-TPR experiments, and the TPR results of all samples are displayed in Figure 6. It can be seen that undoped CeO_2 showed two main reduction peaks centered at around 755 K and 1005 K. According to the literature, the low temperature peak can be ascribed to the reduction of surface-capping oxygen of CeO_2, and the high temperature peak is due to the reduction of bulk oxygen of CeO_2.[12,34–36] Although the reduction peaks of CHS and CZS are poorly resolved in comparison to CPS and CLS samples, all samples exhibited two reduction peaks similar to that of undoped CeO_2. In addition, compared with undoped CeO_2 both the surface and bulk reduction peaks of co-doped samples moved towards the lower temperatures region. Especially, the surface reducibility of the samples followed the order CPS (583 K) > CLS (597 K) > CHS (618 K) > CZS (634 K) > CeO_2 (755 K), which is consistent with the order of BET surface area.

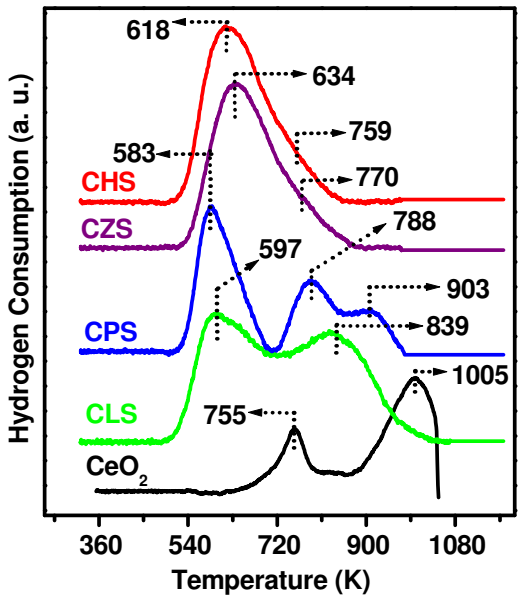

Fig. 6 H_2-TPR profiles of co-doped CeO_2 and undoped (reference) CeO_2 samples.

As the reduction of the surface states leads to the formation of surface oxygen vacancies, the facile formation of surface oxygen vacancies should play an important role in the reducibility of the samples surface. Therefore, the improved surface reducibility of co-doped samples compared with undoped CeO_2 indicates the enhanced mobility of oxygen species in co-doped samples that leads to easier production of oxygen vacancies during the reduction process. In fact, Raman analysis showed the increased oxygen vacancies in co-doped samples as described earlier.

It is thought that the shift of the reduction peak to lower temperatures is caused by the strong interaction between dopants and CeO_2. Especially, since the other dopant cations are hardly reduced, synergistic effect between Ce^{4+}/Ce^{3+} and Sn^{4+}/Sn^{2+} through the redox equilibrium of $2Ce^{3+} + Sn^{4+} \leftrightarrow 2Ce^{4+} + Sn^{2+}$ may play a dominant role.[36,37] However, the largest shift in the surface reduction temperature of CPS than all other samples may be related to the existence of synergistic interaction among all redox couples such as Ce^{4+}/Ce^{3+}, Pr^{4+}/Pr^{3+}, and Sn^{4+}/Sn^{2+}. Besides, the asymmetrical feature of the reduction peak in CPS implies the reduction of -Ce^{4+}-O-Pr^{4+} species along with the -Ce^{4+}-O-Sn^{4+} environment. In summary, H_2-TPR results demonstrated that the co-doping can result in CeO_2 with not only higher surface area but also more active oxygen species.

The chemical states and surface composition of all elements can readily be determined by XPS. XPS analyses are performed in the Ce 3d, O 1s, Sn 3d, Hf 4f, Zr 3d, Pr 3d, and La 3d core levels. Due to the charging effects during XPS analysis, the binding energy values are calibrated using adventitious carbon (284.6 eV). The Ce 3d core level XPS spectra of the samples are presented in Figure 7(A). The fitting of the spectra was carried out using Gaussian profiles. According to widely accepted convention,[9,21,38] Ce 3d spectra could split into ten peaks (five pairs of spin–orbit doublets) which are denoted as u_0, u, u′, u″, u‴ (corresponding to the Ce $3d_{3/2}$ level) and v_0, v, v′, v″, v‴ (corresponding to the Ce $3d_{5/2}$ level). The six peaks (u, u″, u‴, v, v″, v‴) belong to Ce^{4+} species while the other four peaks (u_0, u′, v_0, v′) are related to Ce^{3+} species. In Figure 7(A), all the ten peaks were observed. The result indicates the co-existence of Ce^{4+} and Ce^{3+} ions on the surface of the samples, which is consistent with the results of UV-vis DRS.

In addition, the peaks of co-doped samples are shifted to higher binding energies compared to undoped CeO_2, signifying that the co-doping influences the chemical environment of CeO_2. For all samples, the proportion of Ce^{3+} with regard to the total Ce was calculated from the ratio of the sum of the integrated areas of u_0, u′, v_0, and v′ to the sum of the integrated area of the total ten peaks [$Ce^{3+}/(Ce^{4+} + Ce^{3+})$ ratios]. The corresponding values are listed in Table 1. It can be found that the amount of Ce^{3+} species for all the samples follows the order: CPS (39.2%) > CLS (35.1%) > CHS (32.4%) > CZS (30.8%) > CeO_2 (25.8%). The result suggests that the Ce^{3+} content on the surface of these samples was enhanced by the co-doping of Sn^{4+} together with transition or rare-earth cations.

It is known from the literature that the presence of Ce^{3+} fraction is associated with the formation of oxygen vacancies and the rather high concentration of Ce^{3+} ions on the samples surface evidences a corresponding high amount of oxygen vacancies.[39,40] Moreover, the abundant oxygen vacancies could effectively adsorb reactant gases, which are beneficial for the CO oxidation reaction. Therefore, the highest fraction of oxygen vacancies on the surface of CPS sample (as also observed by Raman and UV-vis DRS results) would be expected to greatly improve its CO oxidation activity among other samples.

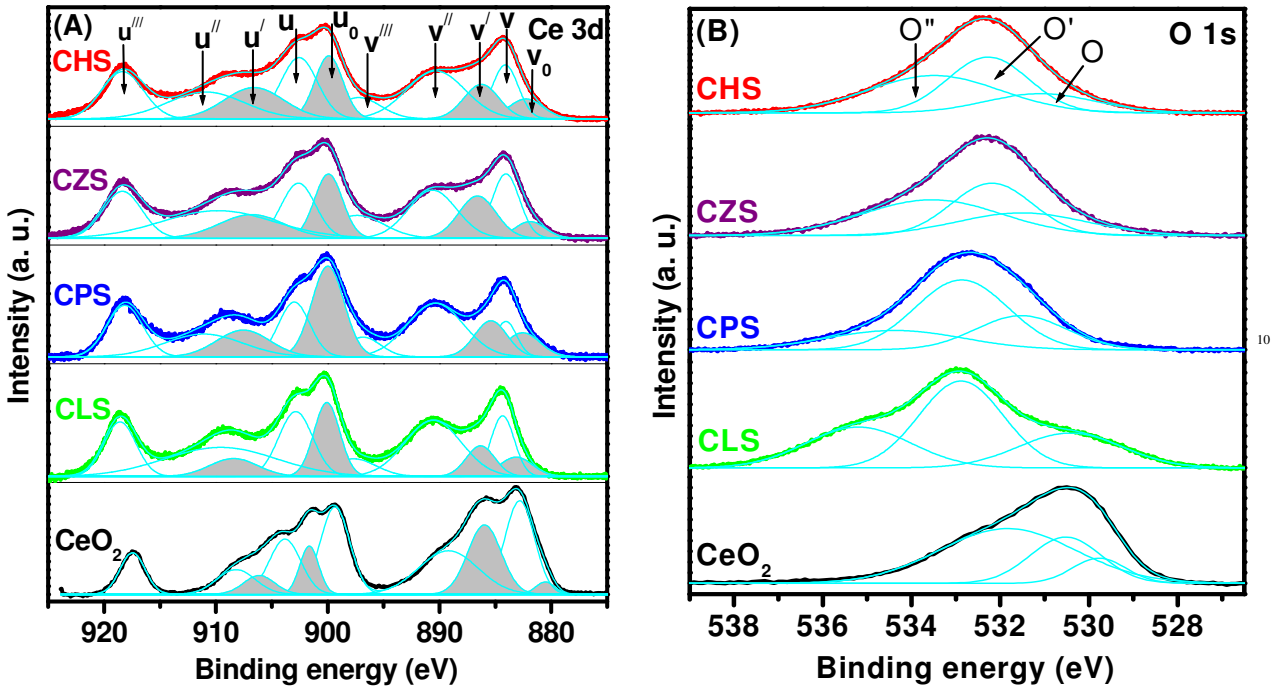

Fig. 7 XPS spectra of (A) Ce 3d (B) O 1s for co-doped CeO_2 and undoped (reference) CeO_2 samples.

Table 1 Crystallite size (D), lattice parameter (a), the position of the main Raman line (F_{2g}), BET surface area (SA), pore volume (V), and the relative quantity of surface adsorbed oxygen species [O′/(O + O′ + O″)%] and Ce^{3+} ions [Ce^{3+}/(Ce^{3+} + Ce^{4+})%] of co-doped CeO_2 and undoped (reference) CeO_2 samples.

Sample	D (nm)	*a* (nm)	Position of F_{2g} (cm^{-1})	SA (m^2/g)	V (cm^3/g)	O′/(O + O′ + O″) %	Ce^{3+}/(Ce^{3+} + Ce^{4+}) %
CHS	8.9	0.5359	467.4	78	0.1454	39.2	32.4
CZS	10	0.5376	466.9	74	0.1452	34.9	30.8
CPS	9.4	0.5387	466.1	95	0.1893	52.9	39.2
CLS	6.3	0.5427	453.3	85	0.1384	48.0	35.1
CeO_2	11.5	0.5400	465.4	41	–	27.1	25.8

To better understand the surface of the samples, the O 1s XPS spectra are compared in Figure 7(B). By deconvolution, the O 1s core level profiles of all the samples can be fitted into three Gaussian peaks. For undoped CeO_2, the peaks are centered at 529.7 eV (thereafter denoted as O), 530.4 eV (thereafter denoted as O′), and 532 eV (thereafter denoted as O″), which are assigned to lattice oxygen species, surface adsorbed oxygen species, and weakly bonded oxygen species like molecular water or carbonates species, respectively.[41–44] However, the peaks of co-doped samples are shifted into higher binding energies than undoped CeO_2. There are two possible reasons; the first is the presence of greater quantities of Ce^{3+} at the surface of the samples,[45,46] which is supported by the Ce 3d results. The second may be that the electronegativity of Sn (1.96) is larger than that of Ce (1.12), Hf (1.30), Zr (1.33), Pr (1.13), and La (1.10) so that the electron affinity of Sn is stronger than that of all other elements, which leads to the higher binding energy of O 1s in CHS, CZS, CPS, and CLS compared with undoped CeO_2 due to the smaller electron density around O element.[36,47]

In addition, O′ oxygen species is believed to be important for oxidation reactions, especially for CO oxidation due to its high mobility compared to O and O″ species.[37,43] The relative concentration ratios of O′/(O + O′ + O″) for each sample were estimated from the areas of O, O′, and O″ peaks and the results are shown in Table 1. It can be noticed that the highest relative content of the O′ was on the surface of CPS (52.9%), followed by CLS (48.0%), CHS (39.2%), CZS (34.9%), and CeO_2 (27.1%). Obviously, it is suggested that the active surface oxygen species should be increased, particularly for CPS sample, by the co-doping of Sn^{4+} along with transition or rare-earth ions into CeO_2 lattice, which can improve the CO oxidation activity. This is in agreement with the H_2-TPR results in which co-doped samples exhibited a surface reduction peak at lower temperature than CeO_2.

The Sn 3d XPS spectrum of co-doped samples is shown in Figure 8. For all the samples, the Sn 3d showed two peaks; one centered at ~486.9 eV, which is typical for Sn $3d_{5/2}$, and the other one at ~495.6 eV, which is attributed to Sn $3d_{3/2}$.[36,48] All these binding energy values are characteristic for Sn^{4+}.[37,49] Interestingly, the $Sn3d_{5/2}$ peak shape is asymmetric and broad, which is probably due to the presence of lower valence state Sn^{2+} and metallic Sn.[37,50] The reason for the generation of Sn^{2+} and Sn^0 may be that the electronegativity of Sn is higher than that of Ce, Hf, Zr, Pr, and La, so the electron can be donated to Sn^{4+}. Furthermore, the coexistence of 4+ and 2+ states of Sn together with the Ce^{4+}/Ce^{3+} redox couple is indicative of the synergistic interaction between Ce and Sn through the redox equilibrium of $2Ce^{3+} + Sn^{4+} \leftrightarrow 2Ce^{4+} + Sn^{2+}$, which may be crucial for the catalytic CO oxidation.[47]

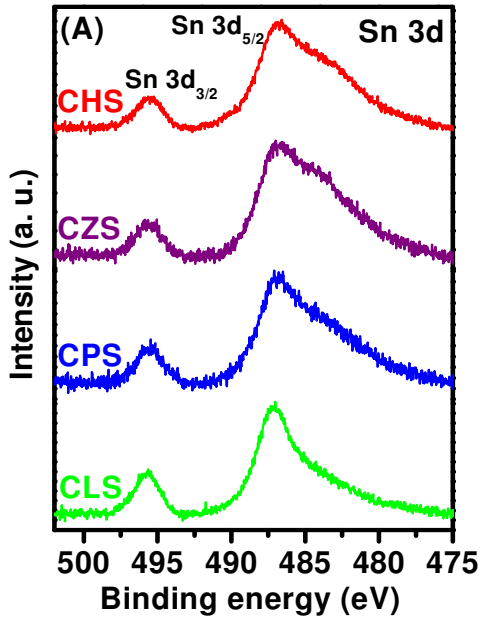

Fig. 8 XPS spectra of Sn 3d for co-doped CeO_2 samples.

The XPS spectra of Hf 4f, Zr 3d, Pr 3d, and La 3d of respective samples are displayed in Figure S2 (ESI†). Hf 4f level normally shows two peaks ($4f_{7/2}$ and $4f_{5/2}$) due to spin-orbit splitting. In order to resolve these peaks, the Hf 4f spectrum was deconvoluted into two components using Gaussian function. It was found that the Hf $4f_{7/2}$ and Hf $4f_{5/2}$ sublevels were at 16.6 and 18.0 eV, respectively.[51] The spin-orbit splitting energy between the two was 1.4 eV, which is in line with the reported values, indicating that Hf existed in 4+ oxidation state.[9,46,52] The deconvoluted Zr $3d_{5/2}$ and Zr $3d_{3/2}$ peaks were observed at about 182.4 eV and 185.0 eV, respectively. The difference in the binding energies between these two components was 2.6 eV, which is in close agreement with the reported value of 2.4 eV.[9] Hence, Zr 3d analysis proved that the Zr is mainly present in a 4+ oxidation state.

The Pr 3d profile exhibited two sets of Pr $3d_{5/2}$ and Pr $3d_{3/2}$ doublets, which were centered at 928.9 and 933.3 eV, and 948.4 and 953.3 eV, respectively. The peaks at 933.3 and 953.5 eV can be attributed to Pr^{4+} and the signals at 928.9 and 948.4 eV may be related to Pr^{3+}, suggesting that the existence of Pr species in the possible 4+ and 3+ oxidation states.[46,53] From the patterns of La 3d core level spectra, it was observed that the BEs of La $3d_{5/2}$ located at the range of 834.2 to 838.4 eV, and the BEs of La $3d_{3/2}$ were at 851.1 to 855.3 eV. The energy splitting observed from the spectra was 4.20 eV, indicating the presence of La^{3+} chemical state, which is well supported by the previous reports.[11,21]

In order to further investigate the oxygen mobility and oxygen vacancies of catalysts, O_2-TPD measurements were carried out. Figure 9 shows the O_2-TPD patterns of co-doped CeO_2 and undoped CeO_2 samples. Two pronounced desorption peaks can be identified over all the samples. The peak at lower temperature (named as α) is corresponding to the desorption of non-stoichiometric oxygen species, such as O^{2-} and O^- adsorbed on the surface oxygen vacancies, and the peak at higher temperature (named as β) can be related to the desorption of lattice oxygen.[54,55] After co-doping of CeO_2, there was a remarkable changes occurred in the O_2 desorption behaviour. Compared to undoped CeO_2, the area of 'α' desorption peak for all co-doped samples is increased. This demonstrates the co-doped samples with good surface oxygen mobility, which should be related to the high concentration of oxygen vacancies as observed by Raman and XPS measurements. Among the samples, the observed larger peak (α) area in CPS suggests the formation of higher number of oxygen vacancies in the sample. It can be seen that the temperature of the peaks (α and β) is shifted to lower values for all co-doped samples as compared to the undoped ceria. Particularly, the shifts in the peak position of 'α' follows the order CPS (584 K) < CLS (593 K) < CHS (612 K) < CZS (616 K) < CeO2 (677 K). These imply that the strong interaction between dopants and CeO_2 in co-doped samples leads to promote the adsorption or mobility or desorption of O_2. Moreover, the highest shift in the peak (α) position of CPS than all other samples probably due to the existence of synergistic interaction among all redox couples such as Ce^{4+}/Ce^{3+}, Pr^{4+}/Pr^{3+}, and Sn^{4+}/Sn^{2+}. These results are well in accordance with the H_2-TPR results. Therefore, both the results of H_2-TPR and O_2-TPD indicated the existence of synergistic interaction between dopants and ceria, which is beneficial for the improved catalytic performance of co-doped samples.

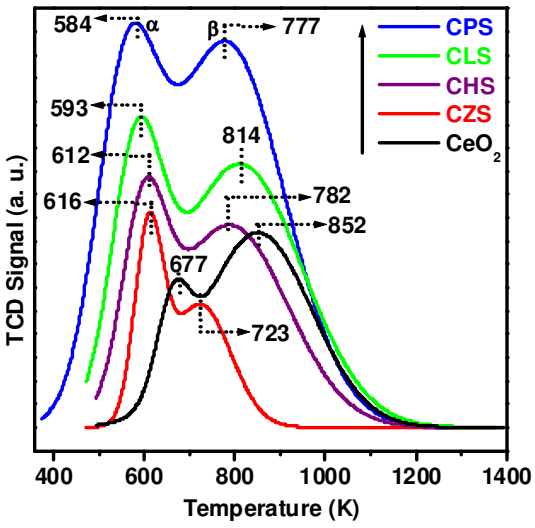

Fig. 9 O_2-TPD profiles for co-doped CeO_2 and undoped (reference) CeO_2 samples.

3.2 CO oxidation activity

The catalytic activity of CZS ternary oxide solid solutions at different molar ratios of Sn and Zr for CO oxidation is provided as ESI† (*see* Figure S3). It is convenient to compare the catalytic activities of the samples by adopting the reaction temperatures T_{50} and T_{90} (corresponding to 50% and 90% CO conversion, respectively). Based on T_{50} and T_{90} values, it was confirmed that the $Ce_{0.80}Zr_{0.12}Sn_{0.08}O_{2-\delta}$ composition of the sample exhibited the highest catalytic activity among the other investigated compositions. Accordingly, the composition of other ternary oxides are fixed at $Ce_{0.80}M_{0.12}Sn_{0.08}O_{2-\delta}$ (M = Hf, Pr, and La) mole ratio.

The CO conversion versus temperature plots of CHS, CZS, CPS, CLS, and CeO_2 samples are shown in Figure 10. In addition, the T_{50} and T_{90} values of various ternary oxide solid solutions are summarized in Table 2. The T_{50} of the samples increased in the order of CPS (523 K) < CLS (539 K) < CHS (549 K) < CZS (565 K) < CeO_2 (714 K). The result illustrated that the T_{50} of CeO_2 is drastically decreased by co-doping and particularly the T_{50} of CPS sample was 191 K lower than the undoped CeO_2. In addition, the T_{90} of the CPS, CLS, CHS, and CZS samples was 578, 622, 647, and 658 K, respectively, but undoped CeO_2 exhibited only 88% conversion even at 798 K. Comparatively, at the T_{90} of CPS, 76%, 67%, 58% conversions are obtained for CLS, CHS, and CZS samples, respectively, while only 6% CO conversion is detected for undoped CeO_2. All these observations clearly demonstrate that the catalytic performance in CO oxidation of CeO_2 is greatly improved by co-doping of Sn^{4+} together with transition or rare-earth ion and the catalytic activity of CPS sample is superior to that of CLS, CHS, CLS, and CeO_2 samples.

It is well-known that the good catalytic activity can be ascribed to the high surface area of the sample which could provide numerous active sites for CO oxidation. According to the results shown in Table 1, the co-doped samples have higher specific surface area compared to undoped CeO_2. The order of BET surface areas of various samples is consistent with the order of CO oxidation activity, indicating that the surface area of the samples is one of the major factors in determining the activity. Besides, H_2-TPR results indicated the enhanced surface reduction ability of co-doped samples than undoped CeO_2, which can be responsible for the improved CO oxidation activity. Especially, surface-capping oxygen species on CPS sample is more readily reduced and consequently, it shows the highest activity among the co-doped samples.

The enhancement in the catalytic activity of the co-doped samples is not only due to their improved surface area and surface reduction ability, but also results from the enriched surface adsorbed oxygen species which can augment the reacting sites for CO oxidation as reported in the literature.[42,56,57] This is clarified by O 1s XPS spectra where the observed trend in relative quantity of surface adsorbed oxygen on the samples is in accordance with the order of activity.

Generally, when CO attaches on the surface of CeO_2, it could react with surface oxygen ions while releasing the CO_2 as an oxidation product and creating oxygen vacancies on the surface. Subsequently, excess electrons are produced on the surface when the oxygen atoms are removed as they hold the negative valence. The excess electrons tend to localize on the surface Ce^{4+} ions and produce Ce^{3+} before filling the oxygen vacancies with gas-phase O_2.[58] The facile formation of Ce^{3+} ions thereby easy creation of oxygen vacancies in the process of CO oxidation can be considered an important factor in determining the catalytic performance of the samples. It is evidenced from the literature that the Ce^{3+} ions or oxygen vacancies significantly increased by the incorporation of Hf, Zr, Pr, and La to CeO_2 lattice.[9–11] When Sn^{4+} co-doped into CeO_2 together with transition or rare-earth ions, the formation of Ce^{3+} ions are further enhanced due to the synergistic interaction between the Ce^{4+} and Sn^{4+} cations through the redox equilibrium of $2Ce^{3+} + Sn^{4+} \leftrightarrow 2Ce^{4+} + Sn^{2+}$. Accordingly, co-doped samples should facilitate the formation of a higher amount of oxygen vacancies than undoped CeO_2 which could improve the CO oxidation activity. More importantly, due to the synergistic effect among all elements redox couples (Ce^{4+}/Ce^{3+}, Pr^{4+}/Pr^{3+}, Sn^{4+}/Sn^{2+}) in the sample, CPS shows the highest number of oxygen vacancies and thus, it exhibits superior activity among the samples. These results are strongly supported from Ce 3d XPS analysis as the order of relative concentration of oxygen vacancies is exactly coincide with activity order of the samples which is also evidenced by Raman and UV-vis DRS studies.

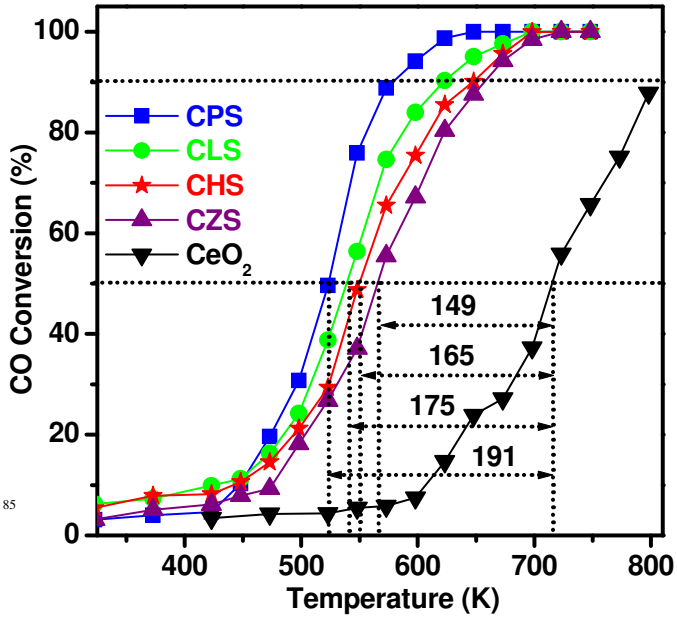

Fig. 10 Catalytic activity of co-doped CeO_2 and undoped (reference) CeO_2 samples for CO oxidation.

In order to know the advantage of CeO_2-based ternary oxide solid solutions over binary oxide solid solutions without Sn dopant, we also compared the activity of present CHS, CZS, CPS, and CLS ternary oxide solid solutions with our previously reported ceria–hafnia (CH), ceria–zirconia (CZ), ceria–proseodymia (CP), and ceria–lanthana (CL) binary oxide solid solutions, respectively, in Figure 11 and Table 2.[9–11] It could be noticed that all ternary oxide solid solutions exhibited better activity than their corresponding binary oxide solid solutions by decreasing the T_{50} and T_{90}. This result clearly suggested that the presence of Sn^{4+} ions in ternary oxide solid solutions significantly

improves the catalytic activity. Among the ternary oxide solid solutions, the T_{50} and T_{90} of CPS sample is 50–171 K and 77–140 K, respectively, lower than the binary oxide solid solutions. This indicates that the excellent CO oxidation activity of CPS than binary oxide solid solutions, which may be again due to synergistic interaction of Ce^{4+}/Ce^{3+}, Pr^{4+}/Pr^{3+}, and Sn^{4+}/Sn^{2+} redox couples.

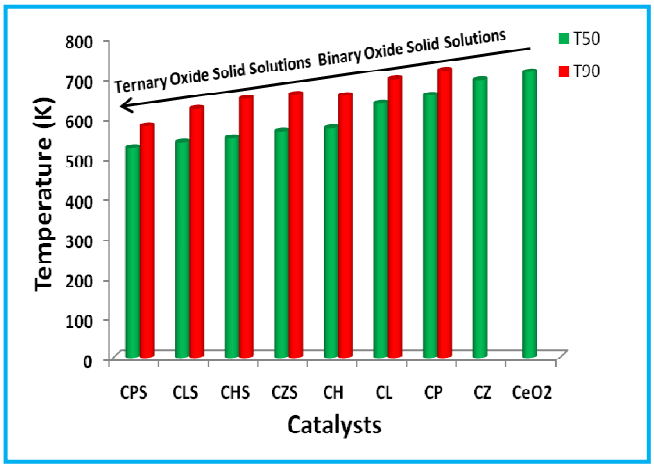

Fig. 11 Comparative study of doped and co-doped CeO_2 samples for CO oxidation.

Table 2 Comparative study of doped and co-doped CeO_2 samples for CO oxidation.

Sample	T_{50} (K)	T_{90} (K)
CHS	549	647
CZS	565	658
CPS	523	578
CLS	539	622
CH	573	655
CZ	694	–
CP	656	718
CL	635	696

4. Conclusions

In the present work, Sn^{4+} and transition or rare-earth ions co-doped CeO_2 ternary oxide solid solutions ($Ce_{0.80}M_{0.12}Sn_{0.08}O_{2-\delta}$, M = Hf, Zr, Pr, and La) were synthesized by coprecipitation method. The correlation between the physicochemical properties and catalytic performance of these co-doped samples for model CO oxidation reaction were attempted. Several conclusions can be draw from this study as outline below:

(1) The co-doping of Sn^{4+} together transition or rare-earth ions into the lattice of CeO_2 resulted in higher surface area compared with undoped CeO_2, which can provide more active sites for CO oxidation.

(2) The co-doped samples showed improved reducibility and enhanced oxygen mobility than undoped CeO_2, which is beneficial to enhance the catalytic activity.

(3) The relative concentration ratios of surface adsorbed oxygen species and oxygen vacancies were significantly increased in the CeO_2 by co-doping process which can play a key role in the CO oxidation reaction.

(4) The superior structural, textural, and redox properties thereby CO oxidation of co-doped samples than undoped CeO_2 attributed to the strong synergistic interaction between the dopants and CeO_2. Among the co-doped samples, the CPS exhibited excellent CO oxidation performance due to synergistic effect of all elements (Ce^{4+}/Ce^{3+}, Pr^{4+}/Pr^{3+}, and Sn^{4+}/Sn^{2+}) redox couples in the sample which may find potential applications in the catalytic oxidation reactions.

Acknowledgments

We gratefully acknowledge Department of Science and Technology (DST), New Delhi for financial support of this work. DD thanks the Department of Education, Australian Government for providing Endeavour Research Fellowship. The authors are also thankful to D. Srikanth, CSIR-NCL, Pune, India for providing O_2-TPD results.

† Electronic supplementary information (ESI) available: Desired quantities of metal precursors for the preparation of co-doped CeO_2 samples, TEM-EDX analysis of co-doped CeO_2 samples, XRD patterns of spent co-doped CeO_2 samples, XPS spectra of Hf 4f for CHS sample, Zr 3d for CZS sample, Pr 3d for CPS sample, and La 3d for CLS sample, and the catalytic activity of the CZS sample at different molar ratios.

Notes and references

[a]*Inorganic and Physical Chemistry Division, CSIR-Indian Institute of Chemical Technology, Uppal Road, Hyderabad-500607, India.*

E-mail: bmreddy@iict.res.in; Fax: +91 40 2716 0921; Tel: +91 40 27193510

[b]*Research School of Engineering, Australian National University, Canberra, ACT 0200, Australia*

[c]*Chemical Engineering Program, School of Energy, Environmental, Biological and Medicinal Engineering, University of Cincinnati, Cincinnati, OH 45221-0012, USA*

References

1 Q. Xie, Y. Zhao, H. Guo, A. Lu, X. Zhang, L. Wang, M.-S. Chen and D.-L. Peng, *ACS Appl. Mater. Interfaces*, 2014, **6**, 421–428.

2 A. Trovarelli, Catalysis by Ceria and Related Materials, Catalytic Science Series; Imperial College Press: London, 2002.

3 H.-T. Chen and J.-G. Chang, *J. Phys. Chem. C*, 2011, **115**, 14745–14753.

4 F. Cova, D. G. Pintos, A. Juan and B. Irigoyen, *J. Phys. Chem. C*, 2011, **115**, 7456–7465.

5 P. Fornasiero, R. D. Monte, G. R. Rao, J. Kašpar, S. Meriani, A. Trovarelli and M. Graziani, *J. Catal.*,1995, **151**, 168–177.

6 J. R. González-Velasco, M. A. Gutiérrez-Ortiz, J.-L. Marc, J. A. Botas, M. P. González-Marcos and G. Blanchard, *Appl. Catal., B*, 1999, **22**, 167–178.

7 P. Fornasiero, G. Balducci, R. D. Monte, J. Kašpar, V. Sergo, G. Gubitosa, A. Ferrero and M. Graziani, *J. Catal.*, 1996, **164**, 173–183.

8 C. E. Hori, H. Permana, K. Y. Simon Ng, A. Brenner, K. More, K. M. Rahmoeller and D. Belton, *Appl. Catal., B*, 1998, **16**, 105–117.

9 B. M. Reddy, P. Bharali, P. Saikia, S.-E. Park, M. W. E. van den Berg, M. Muhler and W. Grünert, *J. Phys. Chem. C*, 2008, **112**, 11729–11737.

10 B. M. Reddy, G. Thrimurthulu, L. Katta, Y. Yamada and S.-E. Park, *J. Phys. Chem. C*, 2009, **113**, 15882–15890.

11 B. M. Reddy, L. Katta and G. Thrimurthulu, *Chem. Mater.*, 2010, **22**, 467–475.

12 J. L. Ayastuy, A. Iglesias-González and M. A. Gutiérrez-Ortiz, *Chem. Eng. J.*, 2014, **244**, 372–381.

13 R. Sasikala, N. M. Gupta and S. K. Kulshreshtha, *Catal. Lett.*, 2001, **71**, 69–73.

14 L. Shi and H. Lin, *Langmuir*, 2011, **27**, 3977–3981.

15 X. M. Yin, C. C. Li, M. Zhang, Q. Y. Hao, S. Liu, Q. H. Li, L. B. Chen and T. H. Wang, *Nanotechnology*, 2009, **20**, 455503.

16 M. A. Mki-Jaskari and T. T. Rantala, *Phys. Rev. B*, 2002, **65**, 245428.

17 J. Yu, D. Zhao, X. Xu, X. Wang and N. Zhang, *ChemCatChem*, 2012, **4**, 1122–1132.

18 X. Wang, J. S. Tian, Y. H. Zheng, X. L. Xu, W. M. Liu and X. Z. Fang, *ChemCatChem*, 2014, **6**, 1604–1611.

19 Q. Dong, S. Yin, C. Guo, T. Kimura and T. Sato, *RSC Adv.*, 2012, **2**, 12770–12774.

20 B. Zhao, G. Li, C. Ge, Q. Wang and R. Zhou, *Appl. Catal., B*, 2010, **96**, 338–349.

21 H. P. Dasari, K. Ahn, S.-Y. Park, H.-I. Ji, K. J. Yoon, B.-K. Kim, H.-J. Je, H.-W. Lee and J.-H. Lee, *Int. J. Hydrogen Energy*, 2013, **38**, 6097–6103.

22 J. R. McBride, K. C. Hass, B. D. Poindexter and W. H. Weber, *J. Appl. Phys.*, 1994, **76**, 2435–2441.

23 B. M. Reddy, A. Khan and P. Lakshmanan, *J. Phys. Chem. B*, 2005, **109**, 3355–3363.

24 P. Fornasiero, J. Kašpar and M. Grazian, *J. Catal.*, 1997, **167**, 576–580.

25 G. Li, Q. Wang, B. Zhao and R. Zhou, *Appl. Catal., B*, 2011, **105**, 151–162.

26 X. Wang, Z. Chen, Y. Wang and R. Wang, *ChemCatChem*, 2014, **6**, 237–244.

27 X. Yao, C. Tang, Z. Ji, Y. Dai, Y. Cao, F. Gao, L. Dong and Y. Chen, *Catal. Sci. Technol.*, 2013, **3**, 688–698.

28 A. Bensalem, F. Bozon-Verduraz, M. Delamar and G. Bugli, *Appl. Catal., A*, 1995, **121**, 81–93.

29 L. Li, F. Chen, J.-Q. Lu, M.-F. Luo, *J. Phys. Chem. A*, 2011, **115**, 7972–7977.

30 Z.-Y. Pu, J.-Q. Lu, M.-F. Luo and Y.-L. Xie, *J. Phys. Chem. C*, 2007, **111**, 18695–18702.

31 Z. Wang, Z. Quan and J. Lin, *Inorg. Chem.*, 2007, **46**, 5237–5242.

32 K. S. W. Sing, D. H. Everett, R. A. W. Haul, L. Moscou, R. A. Pierotti, J. Rouquerol and T. Siemieniewska, *Pure Appl. Chem.*, 1985, **57**, 603–619.

33 G. Leofantia, M. Padovan, G. Tozzola and B. Venturelli, *Catal. Today*, 1998, **41**, 207–219.

34 N. Acerbi, S. Golunski, S. C. Tsang, H. Daly, C. Hardacre, R. Smith and P. Collier, *J. Phys. Chem. C*, 2012, **116**, 13569–13583.

35 D. R. Sellick, A. Aranda, T. García, J. M. López, B. Solsonac, A. M. Mastral, D. J. Morgan, A. F. Carley and S. H. Taylor, *Appl. Catal., B*, 2013, **132–133**, 98–106.

36 X. Yao, Y. Xiong, W. Zou, L. Zhang, S. Wu, X. Dong, F. Gao, Y. Deng, C. Tang, Z. Chen, L. Dong and Y. Chen, *Appl. Catal., B*, 2014, **144**, 152–165.

37 X. Xu, R. Zhang, X. Zeng, X. Han, Y. Li, Y. Liu and X. Wang, *ChemCatChem*, 2013, **5**, 2025–2036.

38 C. Tiseanu, V. I. Parvulescu, M. Boutonnet, B. Cojocaru, P. A. Primus, C. M. Teodorescu, C. Solans and M. S. Dominguez, *Phys. Chem. Chem. Phys.*, 2011, **13**, 17135–17145.

39 J. Fan, X. Wu, X. Wu, Q. Liang, R. Ran and D. Weng, *Appl. Catal., B*, 2008, **81**, 38–48.

40 G. Li, Q. Wang, B. Zhao and R. Zhou, *Fuel*, 2012, **92**, 360–368.

41 Z. Liu, J. Hao, L. Fu and T. Zhu, *Appl. Catal., B*, 2003, **44**, 355–370.

42 Z. Qu, F. Yu, X. Zhang, Y. Wang and J. Gao, *Chem. Eng. J.*, 2013, **229**, 522–532.

43 S. Cai, D. Zhang, L. Zhang, L. Huang, H. Li, R. Gao, L. Shiab and J. Zhang, *Catal. Sci. Technol.*, 2014, **4**, 93–101.

44 J. L. Ayastuy, A. Gurbani, M. P. Gonzalez-Marcos and M. A. Gutierrez-Ortiz, *Int. J. Hydrogen Energy*, 2012, **37**, 1993–2006.

45 D. H. Prasad , S. Y. Park , H.-I. Ji , H.-R. Kim , J.-W. Son, B.-K. Kim , H.-W. Lee and J.-H. Lee, *J. Phys. Chem. C*, 2012, **116**, 3467–3476.

46 D. Harshini, D. H. Lee, J. Jeong, Y. Kim, S. W. Nam, H. C. Ham, J. H. Han, T.-H. Lim and C. W. Yoon, *Appl. Catal., B*, 2014, **148–149**, 415–423.

47 X. Yao, Q. Yu, Z. Ji, Y. Lv, Y. Cao, C. Tang, F. Gao, L. Dong and Y. Chen, *Appl. Catal., B*, 2013, **130–131**, 293–304.

48 T. Baidya, A. Gupta, P. A. Deshpandey, G. Madras and M. S. Hegde, *J. Phys. Chem. C*, 2009, **113**, 4059–4068.

49 P. M. T. M. van Attekum and J. M. Trooster, *Phys. Rev. B*, 1979, **20**, 2335–2340.

50 J. C. Serrano-Ruiz, G. W. Huber, M. A. Sánchez-Castillo, J. A. Dumesic, F. Rodríguez-Reinoso and A. Sepúlveda-Escribano, *J. Catal.*, 2006, **241**, 378–388.

51 C. D. Wagner, W. M. Riggs, L. E. Davis and J. F. Moulder, In Handbook of X-ray Photoelectron Spectroscopy; Muilenberg, G. E., Ed.; Perkin-Elmer Corporation: Eden Prairie, MN, 1978.

52 Y. Wang, Z. Lin, X. Cheng, H. Xiao, F. Zhang and S. Zou, *Appl. Surf. Sci.*, 2004, **228**, 93–99.

53 H. He, H. X. Dai and C. T. Au, *Catal. Today*, 2004, **90**, 245–254.

54 M. Fu, X. Yue, D. Ye, J. Ouyang, B. Huang, J. Wu and H. Liang, *Catal. Today*, 2010, **153**, 125–132.
55 K. Li, H. Wang, Y. Wei and D. Yan, *Int. J. Hydrogen Energy*, 2011, **36**, 3471–3482.
56 Z. Yang, J. Wei, H. Yang, L. Liu, H. Liang and Y. Yang, *Eur. J. Inorg. Chem.*, 2010, **2010**, 3354–3359.
57 Z. Wu, M. Li and S. H. Overbury, *J. Catal.*, 2012, **285**, 61–73.
58 S. Sun, X. Zhao, H. Lu, Z. Zhang, J. Wei and Y. Yang, *CrystEngComm*, 2013, **15**, 1370–1376.